PHYSICAL REVIEW APPLIED **18,** 024063 (2022)

Editors' Suggestion

Broadband Continuous-Variable Entanglement Generation Using a Kerr-Free Josephson Metamaterial

M.R. Perelshtein,[1] K.V. Petrovnin,[1] V. Vesterinen,[2] S. Hamedani Raja,[1] I. Lilja,[1] M. Will,[1]
A. Savin,[1] S. Simbierowicz,[2,†] R.N. Jabdaraghi,[2] J.S. Lehtinen,[2] L. Grönberg,[2] J. Hassel,[2,‡]
M.P. Prunnila,[2] J. Govenius,[2] G.S. Paraoanu,[1] and P.J. Hakonen[1,*]

[1] *QTF Centre of Excellence, Department of Applied Physics, Aalto University, P.O. Box 15100, Aalto FI-00076, Finland*
[2] *QTF Centre of Excellence, VTT Technical Research Centre of Finland Ltd, P.O. Box 1000, FI-02044 VTT, Finland*

(Received 5 June 2021; revised 6 July 2022; accepted 18 July 2022; published 23 August 2022)

Entangled microwave photons form a fundamental resource for quantum information processing and sensing with continuous variables. We use a low-loss Josephson metamaterial comprising superconducting, nonlinear, asymmetric inductive elements to generate frequency-entangled photons from vacuum fluctuations at a rate of 2 giga entangled bits per second spanning over the 4-GHz bandwidth. The device is operated as a traveling-wave parametric amplifier under Kerr-relieving biasing conditions. Furthermore, we demonstrate single-mode squeezing in such devices—3.1 ± 0.7 dB below the zero-point level at half of modulation frequency.

DOI: 10.1103/PhysRevApplied.18.024063

I. INTRODUCTION

The generation of quantum resources—most notably quantum entanglement—is an essential task for the emerging industry employing quantum technologies. While entanglement in discrete variables represents the standard approach for quantum computing, continuous-variable (CV) entanglement between microwave photons is a cornerstone for more robust quantum computing [1–3], sensing [4,5], and communication [6–8] schemes. However, despite extensive technical developments over the past decades, the generation of continuous-variable entanglement lacks efficiency in the microwave range. Thus, it is of great interest to develop ways to generate robust, high-quality entangled states reliably and at a large rate.

The recent progress in quantum optics using microwaves has stimulated widespread interest in parametric Josephson devices that can serve as both quantum limited amplifiers [9–19] and quantum resource generators [20–25]. Such systems, when modulated by an external pump, convert vacuum fluctuations into real photons, creating squeezing between modes at different frequencies symmetric with respect to half of the frequency of the pump—three-wave mixing (3WM), or to the frequency of the pump—four-wave mixing (4WM) [23]. One of the most promising devices of this kind is a traveling-wave parametric amplifier (TWPA) that can operate on a several gigahertz bandwidth [26–29] providing the ability to generate broadband quantum correlations, in contrast to conventional Josephson parametric amplifiers (JPAs) featuring at least an order of magnitude narrower band. These broadband characteristics would, in principle, allow for the operation of a high number of entangled spectrum modes forming a large quantum network [30], which can be used for advanced information processing in the microwave range. However, the performance of real TWPA devices is limited by a high-loss level, impedance mismatching, and a lack of control over nonlinearities [31].

In this work we employ a TWPA where dissipation has been strongly reduced by optimization of the amplification medium. The device allows for adjustable 3WM and 4WM processes. This TWPA has been designed and fabricated at VTT [32]. Using this metamaterial in a Kerr-freed three-wave mixing mode, we report the successful demonstration of vacuum-induced generation of high-quality CV entanglement between frequency-spaced microwaves, reflected also in significant single-mode squeezing.

II. DEVICE

As the TWPA device features a chain of Josephson junction- (JJ) based elements for the realization of a nonlinear inductance, it is instructive to study the effective

---

[*] Corresponding author. pertti.hakonen@aalto.fi

[†] Present address: Bluefors Oy, Arinatie 10, 00370 Helsinki, Finland.

[‡] Present address: IQM Quantum Computers, Keilaranta 19, 02150 Espoo, Finland.

© 2022 American Physical Society

potential energy of a single element [33]

$$U(\varphi) = E_J \left[c_2(\Phi)\varphi^2 + c_3(\Phi)\varphi^3 + c_4(\Phi)\varphi^4 + \dots \right], \quad (1)$$

where E_J is the Josephson energy of one of the constituent junctions, φ is the superconducting phase difference across the element, and Φ denotes the external magnetic flux. Different kinds of Josephson-element topologies result in different expansion coefficients c_n: the c_2 term relates to the critical current and the linear part of Josephson inductance, the c_3 term relates to 3WM and the c_4 term relates to 4WM, which is also known as the Kerr nonlinearity [34,35]. Several topologies have been experimentally proven to work in TWPAs. The simplest one is a single JJ [26,27] $\{c_2, c_3, c_4\} = \{1, 0, -1/12\}$, the natural extension of which is a symmetrical superconducting quantum interference device (SQUID) [36]. To achieve 3WM via a nonzero c_3, we choose Josephson elements known as superconducting nonlinear asymmetric inductive elements (SNAILs) with one small, αE_J, junction on one side and $n = 2$ large, E_J, junctions on the other side [33]. The asymmetry ratio $\alpha < 0.5$ ensures that the element exhibits only a single potential minimum.

One critical aspect of TWPAs is the need for phase matching [37], which was achieved in 4WM TWPAs using resonant matching [36,38], or changing the sign of the Kerr nonlinearity [39,40]. However, the presence of a strong pump at the center of the gain band in 4WM TWPAs is a potential source of back action. In practice, the quantum efficiency and output field squeezing are also limited by the Kerr-type nonlinearity [41]. Besides that, the generation of higher-order harmonics products, increasing the losses in the TWPA [42], could lead to substantial degradation of the entanglement and squeezing performance.

Addressing these issues, our TWPA is a coplanar waveguide (CPW) transmission line where a SNAIL array center conductor simultaneously suppresses the Kerr mixing term and ensures 50Ω impedance matching, while retaining a sufficient degree of 3WM. In contrast to Ref. [40] where an alternating polarity of SNAIL-like elements suppresses 3WM, our SNAILs [Fig. 1(b)] have the same dipolar orientation throughout. We realize homogeneous flux biasing for all the 1632 SNAILs, and negligible off-chip fringing fields, using a magnetic flux bias line placed on chip. The details of the unit-cell design that is shown in Fig. 1(a) are presented in Ref. [32] and the Appendix A. Resistors keep the flux bias line [depicted in blue in Fig. 1(a)] grounded at microwave frequencies, thereby acting as the L/R low-pass filter and blocking microwave propagation along it. The scheme also contributes towards keeping the two sides of the CPW ground at the same potential. At the same time, the resistors prevent leakage of the static current and the formation of parasitic loops of quantized magnetic flux. The resistance value is chosen to be much lower than the reactance of the unit-cell shunt capacitor at signal, idler, and pump frequencies—1200, 1200, and 600 times, respectively. The resistors thus contribute to the effective loss tangent of the shunt (quantified below), which, however, remains dominated by dielectric loss.

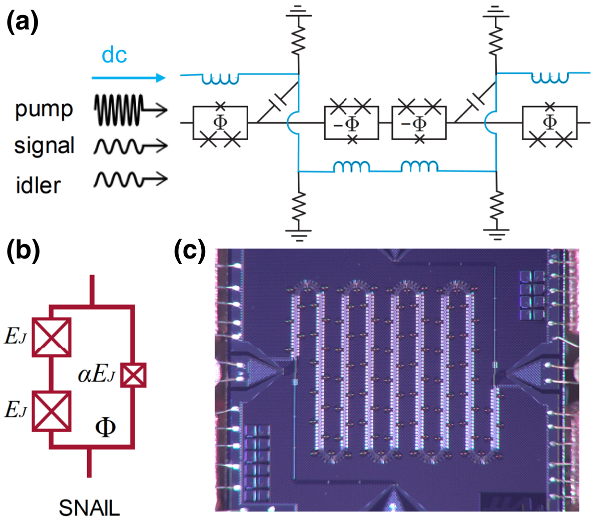

FIG. 1. (a) Coplanar waveguide transmission line where the center conductor is composed of Josephson elements called superconducting nonlinear asymmetric inductive elements (in black). The dc tuning lines (in blue) are used to change the effective inductance of the TWPA. The pump and the signal are combined at the same input port. (b) The scheme of SNAIL that provides control over mixing processes via external magnetic flux. (c) Optical photograph of the bonded device with chip size 5×5 mm^2. The device features four ports: left and right ports are used for the microwaves' input and output and top and bottom additional ports are used for the dc input and output.

The device [Fig. 1(c)] is fabricated with a side-wall passivated spacer niobium junction technology detailed in Refs. [43,44]. At zero-flux bias, the characteristic impedance of the TWPA is far below the optimal value of 50Ω and the SNAIL nonlinearity does not allow for 3WM. Ramping up the bias into the regime near $\Phi = 0.4\Phi_0$, where Φ_0 is magnetic flux quantum, improves the impedance matching, and the SNAILs exhibit 3WM combined with only weak 4WM. The weakened 4WM contributes favorably to the phase matching of the amplification process and to nonclassical state generation.

In a linearly dispersive TWPA, the 3WM would strongly and unidirectionally convert pump power into higher harmonics [45]. At angular frequencies higher than the pump (ω_p), our TWPA has nonlinearly dispersive features primarily from the combination of Josephson plasma resonance and the periodic loading of the CPW with dispersive capacitors [38,46]. We control the phase mismatch of the second-harmonic generation (SHG) [47] in particular. Instead of blocking SHG altogether we allow a weak and cascaded mixing process where the pump accrues a favorable phase shift when converting from ω_p to $2\omega_p$ and later back to ω_p [48]. The phase shift looks effectively like 4WM and contributes to the compensation of the Kerr effect within the device. The pump frequency is a degree of freedom that allows us to explore different levels of SHG and, consequently, to optimize the pump-phase shift [46]. More details can be found in the Appendix B.

Our device provides 15.3 dB of gain over a 3-GHz bandwidth with the noise temperature being close to the single-photon quantum limit. The results on TWPA characterization as a quantum limited amplifier are presented in the Appendices C and D. Although our loss tangent of about 0.003 is not particularly low, 3WM requires a shorter transmission-line length for the same amount of gain as 4WM [28]. At our frequency of interest 4.8 GHz, the unpumped TWPA shows about 0.6 dB of loss (see Appendix F), which is to be contrasted against 2.4 dB and 3.0 dB extrapolated from Refs. [36,49]. Such a low-loss level is the key feature that allows us to generate entangled quantum states and achieve squeezing.

III. EXPERIMENTAL SETUP

The experimental scheme for TWPA-based entanglement generation is presented in Fig. 2. The pump signal $\omega_p = 2\omega$ enters the TWPA at 20-mK temperature through the chain of attenuators and triggers the generation of correlated photons in the frequency bands $\Delta_L = [\omega - \Delta\omega - \delta\omega : \omega - \Delta\omega]$ and $\Delta_R = [\omega + \Delta\omega : \omega + \Delta\omega + \delta\omega]$ generated from vacuum fluctuations [23]. Here, $\Delta\omega$ is band detuning from frequency ω, and $\delta\omega$ is the bandwidth that is set manually and can be specified according to the goals. In our experiment, $\omega = \omega_p/2 = 2\pi \times 4.8$ GHz, $\delta\omega = 2\pi \times 0.5$ MHz and band separation $2\Delta\omega$ is varied from 0, the case of minimal mode separation, up to $2\pi \times 4$ GHz, the maximum mode separation allowed by the bandwidth of our experimental setup. Both ω and 2ω signals exit the TWPA, but only a filtered sub-band of 4–8 GHz microwaves are amplified using the HEMT and room-temperature amplifiers. We record signals using dual-readout configuration, which simultaneously demodulates the bands with two separate *IQ* mixers [22] that are then digitized with a multichannel Alazar ATS9440 digitizer.

IV. ENTANGLEMENT CHARACTERIZATION

We characterize the entanglement in N-mode output quantum state using the covariance formalism. According to the theory of parametric amplifiers, all output states are Gaussian [50,51]. We verify this assumption by measuring the skewness and kurtosis that prove the Gaussian nature of the signals (see Appendix G). The state is fully characterized by the covariance matrix $\mathbf{V}$ of the I and Q voltage quadratures of the propagating microwave modes $1, \ldots, N$:

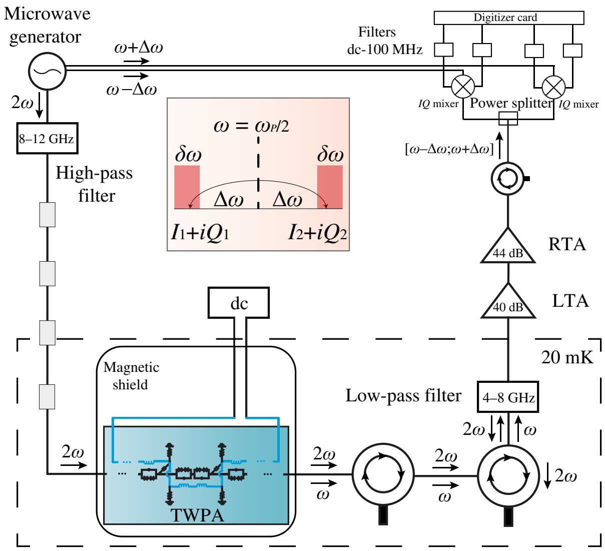

FIG. 2. Measurement scheme for entanglement generation and verification. The microwave pump at frequency 2ω enters the TWPA through the chain of filters and attenuators and triggers the generation of correlated photons. The TWPA is biased with a magnetic flux via the dc line. The pump signal is filtered out with a band-pass filter, while the 4–8 GHz microwaves are amplified with a chain of low-temperature and room-temperature amplifiers, LTA and RTA, respectively. The output signal in $[\omega_p/2 - \Delta\omega; \omega_p/2 + \Delta\omega]$ range is split into two branches using a power splitter. The two branches are demodulated with separate local oscillators to symmetric frequency bands. Outputs of the *IQ* mixers are then filtered to avoid aliasing effects, after which the signals are digitized with an Alazar digitizer card. The scheme of the generation of frequency-entangled microwaves is presented in pink embedding. Two modes Δ_L and Δ_R with $\delta\omega$ bandwidth are shifted by $\Delta\omega$ from the $\omega_p/2$ frequency.

$$
\begin{aligned}
K &= (I_1, Q_1, \ldots, I_N, Q_N)^T, \\
V_{ij} &= \langle K_i K_j + K_j K_i \rangle / 2.
\end{aligned}
\tag{2}
$$

Before the covariance matrix analysis, we calibrate the quadratures in order to be able to compare the variances and covariances to the vacuum noise level, which is crucial for the entanglement verification. We convert quadrature voltages I and Q to the scaled quadratures $\mathcal{I}$ and $\mathcal{Q}$ in the following way:

$$
\begin{aligned}
\langle \mathcal{I}_i^2 \rangle &= \frac{\langle I_i^2 \rangle_{\text{on}} - \langle I_i^2 \rangle_{\text{off}}}{\mathcal{N}} + \frac{1}{4}, \\
\langle \mathcal{I}_i \mathcal{I}_j \rangle &= \frac{\langle I_i \, I_j \rangle_{\text{on}}}{\mathcal{N}},
\end{aligned}
\tag{3}
$$

with the same transformation applied to $\mathcal{Q}$. Here, the normalization coefficient $\mathcal{N}$ is given by

$$
\mathcal{N} = \frac{G_{\text{sys}} Z_0 h f \, \text{BW}}{4\eta},
\tag{4}
$$

where G_{sys} is measured system gain, $Z_0 = 50\Omega$, h is Planck's constant, f is operating frequency, BW is the measurement bandwidth, and η represents internal losses of the TWPA. We rescale the vacuum fluctuations to unity for analysis. Details on system gain calibration and rigorous analysis of quantum modes propagating in the TWPA within distributed gain and loss model are presented in the Appendices E and F.

Our entanglement analysis employs the Peres-Horodecki criterion of positivity under partial transpose (PPT) [52,53] based on symplectic transformation of the covariance matrix [54]. In a further analysis, we use the logarithmic negativity [55], $E = \max[-\log_2 \nu_{\min}, 0]$, that constitutes an upper bound to the distillable entanglement of the state and corresponds to the entanglement cost under PPT preserving operations [56]. Here $\nu_{\min}$ is a minimum symplectic eigenvalue. Considering the scaled quadratures, which correspond to vacuum fluctuations equal to 1 (see Appendix G), E is nonzero only if $\nu_{\min} < 1$, and it quantifies the quantum information capacity of the entangled state. We want to emphasize that the low-loss level is crucial for the entanglement generation since the internal loss parameter η defines the normalization coefficient $\mathcal{N}$, which, in turn, affects the minimum symplectic eigenvalue.

V. ENTANGLEMENT GENERATION

We characterize our results on two-mode ($N = 2$) entanglement in terms of logarithmic ($\log_2$) negativity. Figure 3(a) displays E as a function of pump power for two different separations of Δ_L and Δ_R modes. Mixers used for the downmixing of output signals in the measurement scheme introduce correlations that have a classical nature with $E_0 \approx 0.1$. Since E is an additive quantity, we subtract E_0 measured at -110 dBm from the data resulting in $E = 0$ at low powers that indicates an uncorrelated ground state of the metamaterial. With increasing of pump power, the logarithmic negativity reaches 0.85 ± 0.20 for nonspaced modes at -69-dBm power as shown in the left frame in Fig. 3(a). For modes with 2-GHz spacing, we observe similar behavior with the same maximum logarithmic negativity indicated in the right frame in Fig. 3(a). With further increase in pump power, the entanglement disappears since high drive power introduces detrimental higher-order couplings and wave-mixing processes [57]. Similar behavior has been observed in transmission lines terminated by a SQUID [25] and lumped-element JPAs [41]. In order to prove the nonideality of the state at higher pump powers, we show the decline of purity, calculated for Gaussian states [58], in Fig. 3(a) for both spaced and nonspaced modes.

To demonstrate the broadband entanglement generation we fix the pump frequency and analyze the maximum E as a function of the separation of modes, see Fig. 3(b), and verify the entanglement generation over the 2-GHz bandwidth, which is limited by the experimental scheme. In order to generate entanglement over the whole 4-GHz bandwidth, we change the pumping frequency

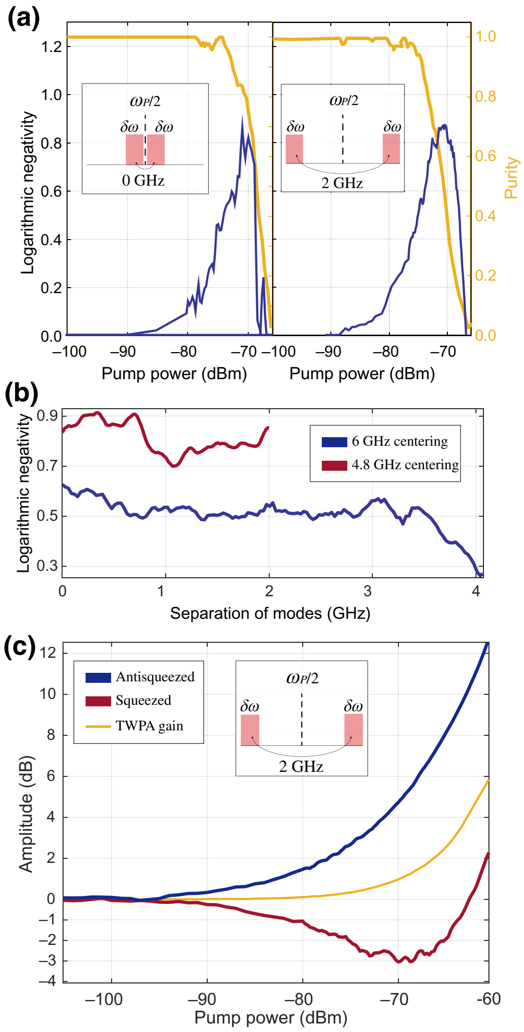

FIG. 3. (a) Logarithmic negativity E and purity as a function of the pump power with $\omega_p = 2\pi \times 9.6$ GHz. Nonzero negativity indicates the presence of entanglement. Negativity for nonspaced frequency bands is depicted in the left frame, while negativity for 2-GHz mode separation is shown in the right frame. The purity is shown in yellow: as purity fades, the entanglement disappears. The insets show the frequency-mode definition. (b) Maximum logarithmic negativity as a function of the separation of modes with optimized pump power for two-pump frequency $\omega_p = 2\pi \times 11.98$ GHz (in blue) and $\omega_p = 2\pi \times 9.6$ GHz (in red). While pumping at $\omega_p = 2\pi \times 9.6$ GHz allows for the higher logarithmic negativity, the center of the operating band is not in the center of the experimental band, which limits the separation of modes. In the case of $\omega_p = 2\pi \times 11.98$ GHz, the entanglement is preserved over the whole 4-GHz bandwidth. (c) Two-mode squeezing for different pump powers in the case of $\omega_p = 2\pi \times 9.6$ GHz. Amplified S_- quadrature is depicted in blue, squeezed S_+ quadrature is depicted in red. The gain of the TWPA is shown in yellow.

$\omega = \omega_p/2 = 2\pi \times 5.99$ GHz so that the half of the pump is at the center of the measurement band. Such a change in pump frequency degrades impedance matching, resulting in a lower logarithmic negativity value, as demonstrated in Fig. 3(b). The internal losses and the system gain is measured and calibrated over the whole 4–8-GHz bandwidth. As can be seen, the logarithmic negativity is nearly constant and starts to decrease only near the bandwidth limit of the experimental setup.

To illustrate the excellent quality of our metamaterial, we demonstrate the generation of vacuum-induced squeezed states. For this experiment, we consider two modes with 2-GHz spacing centered at $\omega_p/2$. The parametric amplifier operates in the degenerate mode at this point. Measuring and calibrating I and Q quadratures in the same way as for two-mode entanglement verification, we introduce $S_+ = \langle \mathcal{I}^2 \rangle$ and $S_- = \langle \mathcal{Q}^2 \rangle$ amplitudes that correspond to squeezed and amplified quadratures with respect to the vacuum level. These amplitudes are shown in Fig. 3(c) as a function of the pump power. The maximum squeezing of 3.1 ± 0.7 dB is achieved at −69-dBm pump power. Higher powers introduce nonlinearities that distort the quantum state and reduce the squeezing, similarly to what occurs for resonant Josephson parametric amplifiers [41]. The same level of squeezing is observed for the single-mode experiment and is presented in the Appendix J.

In order to quantify our TWPA as a generator of entangled photon flux, we define an entanglement generation rate

$$R_E = 2\langle \mathcal{I}_1^2 \rangle E_F(\Delta\omega + \delta\omega) \tag{5}$$

that quantifies the production rate of available quantum information. Here, $\langle \mathcal{I}_1^2 \rangle$ is the estimation on the photon flux intensity [approximately $1/(s$ Hz$)$], E_F is the entropy of formation in ebits [59] and $2(\Delta\omega + \delta\omega)$ is the effective bandwidth of the frequency span in which photons are generated from vacuum fluctuations. The entropy of formation quantifies how many Bell states are needed to prepare the given state using local operations and classical communications, and it is calculated from the minimum symplectic eigenvalue $\nu_{\min}$ detailed in the Appendices H and I. In contrast to the discrete-variables case where the number of qubits defines the entanglement strength, we define the entanglement with respect to an arbitrary number of spectrum modes within the device bandwidth. Therefore, R_E is proportional to the bandwidth as well as to the amount of two-mode squeezing between the pairs of frequencies.

We find that our device provides at least 2 Gebits/s (giga entangled bits per second) over 4 GHz, being limited by the working band of the experimental setup. Outside of the 4–8-GHz band, the signal is cut off by circulators, bandpass filters and the bandwidth of the HEMT amplifier, making the entanglement verification impossible at these frequencies. A similar JPA-based entanglement generation scheme featuring 5 dB of squeezing ($\nu_{\min} = 0.33$) and 5-MHz bandwidth [22] can provide only 6 Mebits/s—3 orders of magnitude lower value.

VI. CONCLUSION

In summary, we demonstrate a broadband SNAIL Josephson traveling-wave parametric amplifier for generation of nonclassical states. Owing to low losses in our 3WM TWPA design, we are able to generate entangled microwave signals over the 4-GHz bandwidth, and with $E = 0.85 \pm 0.20$ maximum logarithmic negativity with optimized pumping. For single-frequency mode of operation, we reach 3.1 ± 0.7 dB of quantum squeezing. Higher entanglement generation rate and squeezing can be achieved by further improving the experimental scheme and the TWPA, mainly impedance matching, reducing dielectric losses and dissipation by resistance, and suppressing the Kerr nonlinearity.

Finally, the results presented in this work hold high promise in meeting the challenges of broadband quantum information processing with continuous-variable (CV) states. Indeed, the Kerr effect can be employed in realizing universal quantum gates for CV quantum computing [60–62]. In Josephson microwave circuits, Kerr effects are much stronger than in optical systems, and, with the excellent engineering of nonlinearities demonstrated in this work, these proposals may turn out to be realizable. As we demonstrate, the broadband features of the TWPA allow operation over few gigahertz bandwidth, and in combination with the multiple pumping scheme [63] pave the way towards generation of frequency-spaced multimode entanglement. Multimode schemes can be employed for various quantum applications, such as CV computing with cluster states [64], secure and robust communications [65], distributed quantum-limited sensing [66], and search for dark matter [67].

ACKNOWLEDGMENTS

We thank Alpo Ahonen, Paula Holmlund, and Harri Pohjonen for technical assistance and Terra Quantum AG for scientific support. K.V.P. is funded by the European Union's Horizon 2020 research and innovation programme under Grant Agreement No. 862644 (FET-Open project: Quantum readout techniques and technologies, QUARTET). The work at VTT is funded from the EU Flagship on Quantum Technology Grant No. H2020-FETFLAG-2018-03 Project Nos. 820363 OpenSuperQ and 820505 QMiCS. The contribution of M.R.P., I.L., M.W., and A.S. is supported by Grant Agreement No. 824109 (European Microkelvin Platform project, EMP), and ERC Grant Agreement No. 670743 (QuDeT). P.J.H. and V.V. acknowledge financial support from the Academy of Finland through Grants No. 314448 and No. 321700, respectively. The work of S.H.R. and P.J.H. is supported by a MATINE research grant. G.S.P. and K.V.P. thank Saab for scientific collaboration under a research agreement with Aalto University. This work is done under the "Finnish Center of Excellence in Quantum Technology QTF" of the Academy of Finland, Projects No. 312059, No. 312294, No. 312295, No. 336810, and No. 312296.

Note added.—Recently, we became aware of the works on squeezing and entanglement generation in TWPAs [68,69].

APPENDIX A: DETAILS OF TWPA DESIGN AND FABRICATION

The TWPA is realized with VTT's multilayer superconductive fabrication process [43,44], where the metal and insulator thicknesses vary between 50–200 nm. The fabrication on a high-resistivity silicon wafer begins with the deposition and patterning of a Nb/Al-AlO$_x$/Nb trilayer. We use strips of the trilayer in the SNAILs (110) in Fig. 4. Whenever the subsequent main wiring layer of niobium crosses with a strip, a Josephson junction will form at the crossover.

The ground planes (101) of the CPW are made of the main wiring layer. The main wiring layer also has dispersive capacitors [open-ended transmission-line spiral resonators [46,70] with one side galvanically connected to the CPW center conductor (140) and the other side to the ground] as well as the bottom electrodes of parallel-plate capacitors (120). The capacitance of a single SNAIL is 28.3 fF, which is not constant along the length of the transmission line. Next, we uniformly cover the device with atomic layer deposited aluminum oxide insulator. We make contact holes to the insulator at the forthcoming sites of resistors (150), for instance. We cover the insulator with a secondary niobium wiring layer that is used for the magnetic flux bias line (130). The flux line has a meander shape and it repeatedly crosses from one side of the CPW to another. Notably, the flux line also serves as the top electrode of the parallel-plate capacitors (120) [32]. The final fabrication step is the deposition and patterning of a normal-metal resistive layer. The resistors (150) connect the flux line on the secondary wiring layer to the ground (101) on the main wiring layer. The circuits parameterized are outlined in Refs. [32,46].

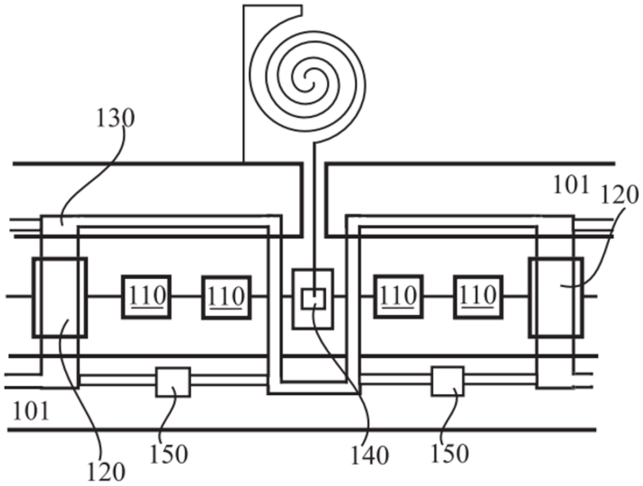

FIG. 4. A top-view sketch of the TWPA layout on the chip.

For details on managing the higher harmonic generation of the pump frequency, we refer to Ref. [46]. In brief, we arrange a TWPA dispersion curve that is superlinear at the SHG frequency of the pump. The SHG, which is inherent to 3WM, is phase mismatched and the frequency-doubled microwaves are downconverted with a shifted phase. This refractive effect, which resembles the Kerr effect in 4WM, is well known in the field of nonlinear optics [48]. The primary origin of the superlinear dispersion is a stopband near the SHG frequency, induced by the periodic loading of the TWPA with the spiral resonators. The first stopband from the loading occurs when the distance between the spirals corresponds to half a wavelength [38]. The dispersive effects of the spiral resonator eigenmode and the Josephson plasma frequency are responsible for the phase mismatching of any higher-order nonlinear processes above the SHG frequency.

The reflection coefficient of the unpumped TWPA is shown in Fig. 5 for different voltage bias values and probe frequencies. The coefficient is normalized with respect to an open circuit at the mix plate.

APPENDIX B: CONTROL OF THE WAVE-MIXING PROCESS IN TWPA

To address the nonlinearity of the device, we first derive the potential energy of a single SNAIL. We denote the phase of the smaller Josephson junction by φ_s, and the total phase of the SNAIL (traversing around the loop) by $\varphi_{\text{ext}} = 2\pi\Phi/\Phi_0$. With uniform phase drop across the two large junctions, transport current of the SNAIL reads $I = \alpha I_c \sin\varphi_s - I_c \sin(\varphi_{\text{ext}} - \varphi_s)/2$, where I_c is the critical current. Having the voltage-phase relation $V = \Phi_0/2\pi\dot{\varphi}$, one obtains the potential energy of the SNAIL by

$$U_S(\varphi_s) = E_J \int \left(\alpha I_c \sin\varphi_s - I_c \sin\frac{\varphi_{\text{ext}} - \varphi_s}{2}\right)\dot{\varphi}_s = - \alpha E_J \cos\varphi_s - 2E_J \cos\frac{\varphi_{\text{ext}} - \varphi_s}{2}, \tag{B1}$$

with $E_J = \Phi_0 I_c/2\pi$. Assume now that U_S has a minimum at a phase denoted by $\varphi_{\min}$. We Taylor expand the potential energy around this point, such that with $\tilde{\varphi} = \varphi_s - \varphi_{\min}$ we have

$$U_S(\tilde{\varphi})/E_J = c_1\tilde{\varphi} + c_2\tilde{\varphi}^2 + c_3\tilde{\varphi}^3 + c_4\tilde{\varphi}^4 + \dots, \tag{B2}$$

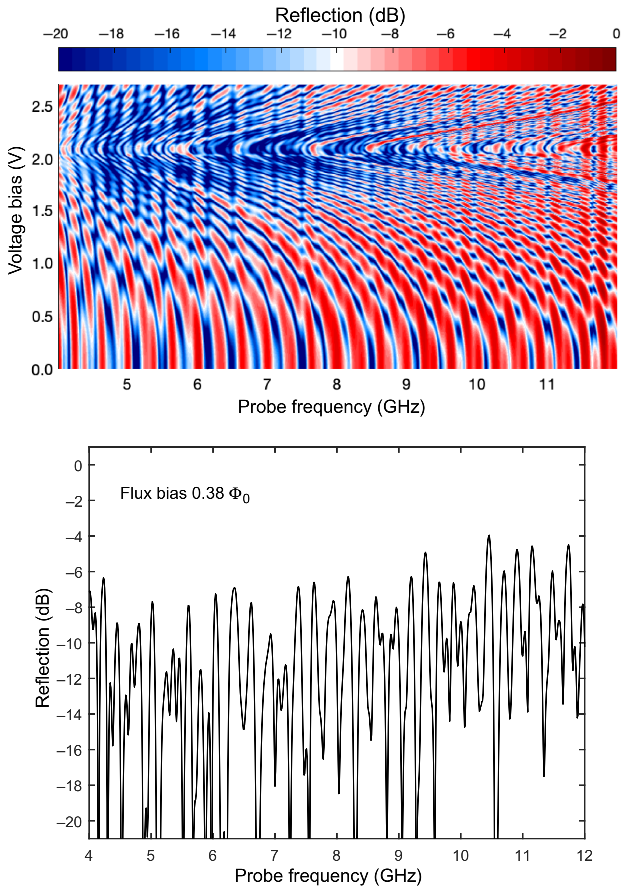

FIG. 5. Top: reflection coefficient as a function of the probe frequency and voltage bias. Bottom: reflection coefficient as a function of the probe frequency at a working flux bias of $0.38\Phi_0$.

where $c_n = (1/n!E_J)d^nU_S(\varphi_s)/d\varphi_s^n|\varphi_{\min}$. Sitting at the minimum of U_S means that $c_1 = 0$, i.e., the transport current of SNAIL is zero. The coefficients $c_n(\varphi_{\text{ext}})$ and the Josephson inductance $L_J = \Phi_0/2\pi I_c$ completely determine the behavior of a SNAIL. However, having an array of SNAILs embedded in a transmission line is more involved and requires careful consideration of the nonlinear current conservation. Here, we follow the results presented in Ref. [71] to address this issue and to estimate the nonlinearity of our device, which determines 3WM and 4WM. Consider a simple lumped-element model in which an array of M SNAILs are placed in series with a linear inductance L and capacitance C. Taking φ as the canonical phase coordinate for the mode, the potential energy of the whole circuit reads

$$U_T(\varphi,\varphi_s) = MU_S(\varphi_s) + \frac{1}{2L}\varphi_0^2(\varphi - M\varphi_s)^2, \tag{B3}$$

where φ_0 is the reduced flux quantum. As explained in Ref. [71], the SNAIL phase φ_s is no longer an independent coordinate and needs to be treated as a function of the phase coordinate φ. This can be achieved by accounting for the nonlinear current conservation for the node between the array of SNAILs and the linear inductance:

$$\alpha I_c \sin\varphi_s + I_c \sin\frac{\varphi_s - \varphi_{\text{ext}}}{2} + I_c\frac{L_J}{L}(M\varphi_s - \varphi) = 0. \tag{B4}$$

Taking into account $\varphi_s[\varphi]$, Taylor expansion of the total potential energy U_T around a minimum determined by $\bar{\varphi}_{\min}$ yields the coefficients $\tilde{c}_n$, which are related to the corresponding coefficients for a single SNAIL [71]:

$$\tilde{c}_2 = \frac{p}{M}c_2, \tilde{c}_3 = \frac{p^3}{M^2}c_3, \tilde{c}_4 = \frac{p^4}{M^3}\Big(c_4 - \frac{9c_3^2}{4c_2}(1-p)\Big), \tag{B5}$$

with $p = ML_J/L/2c_2 + ML_J/L$. 4WM is connected to $\tilde{c}_4$ (Kerr term). According to the expressions above, this term is dependent on c_3^2 in addition to c_4. Therefore, a vanishing c_4 does not appear to be sufficient for a Kerr-free situation.

The results of the simple lumped-element model may not be directly applicable to a TWPA as such, but we expect that basically similar observations will hold for coupled-mode equations [28,38] describing the waves propagating in the TWPA. All through the TWPA operation, it is useful to keep in mind that the effective Kerr coefficient depends not only on c_4 but also on a term proportional to c_3^2. As a consequence, we take both c_3 and c_4 into account for optimizing the device. The coefficients c_3 and c_4 are shown in Fig. 6 for various flux and SNAIL asymmetry values. 3WM requires a magnetic flux $0 < |\Phi| < 0.5\Phi_0$, where Φ_0 is the magnetic flux quantum. Note that $c_3(-\Phi) = -c_3(\Phi)$, while $c_4(-\Phi) = c_4(\Phi)$.

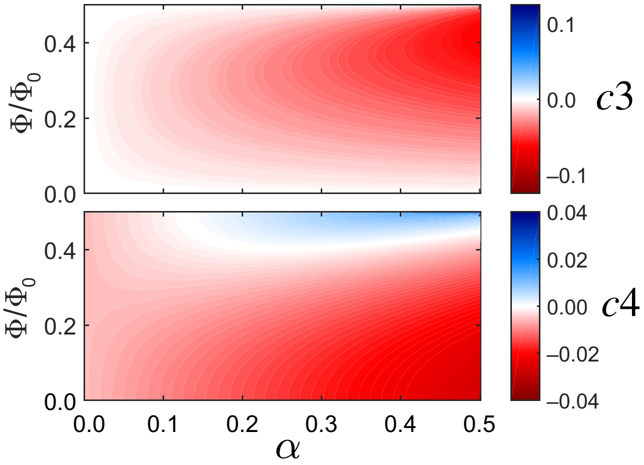

FIG. 6. The dependence of c_3 and c_4 coefficients of a SNAIL on the applied magnetic flux and SNAIL asymmetry α.

APPENDIX C: MEASUREMENT SETUP

The TWPA is cooled down in a dry dilution refrigerator BlueFors LD400 with 10 mK base temperature. The nonmagnetic package for TWPA is made of a copper base, an aluminum lid, and brass connectors with two SMP ports for microwaves and two MMCX ports for the on-chip flux line. The pump signal was generated by ANAPICO APMS12G 4-channel signal generator with -150 dBc/Hz phase noise at 100 kHz. The pump signal is band-pass limited to the 8–12-GHz range with mini-circuit filters to ensure suppression of ω signal and is thermalized by a chain of attenuators, -60 dB altogether. The dc signal is generated by a Stanford SIM928 Isolated Voltage Source, filtered and routed to flux loops by a superconducting twisted pair cable. In order to guide the signals to the output, we use low-noise factory circulators 4–12 GHz operating as isolators. The filtered signal in 4–8-GHz range is first amplified by a cooled Low Noise Factory LNC4 8C HEMT amplifier (40 dB of gain and 4-K noise temperature), connected using a BeCu coaxial cable and SMA connectors to a room-temperature amplifier with 44-dB gain. The microwaves are captured with the four-channel 14-bit Alazar ATS9440 digitizer with 125 MS/s rate.

APPENDIX D: TWPA CHARACTERIZATION

First, we characterize our device from the perspective of broadband low-noise parametric amplifier in a dry dilution refrigerator at $T = 20$ mK. For this purpose, we probe the TWPA with a weak microwave signal (-120 dBm) and apply a pump through the same port, and record the amplified signal. We characterize the amplification performance by measuring the mean gain value normalized against the superconducting transmission line placed in the TWPA's sample holder over 4–8-GHz frequency range. The best gain performance of the device is observed at a static flux bias of $\Phi = 0.38\Phi_0$: the mean gain is depicted in Fig. 7(a) for various pump powers and frequencies. Choosing the best operating point with the pump frequency 9.6 GHz and the pump power -63 dBm [marked with the blue star in Fig. 7(a)] we evaluate the gain profile depicted in Fig. 7(b). The 1-dB compression point indicates the input saturation power of the amplifier is -100 dBm for 20-dB gain.

The noise performance of the TWPA is characterized using the signal-to-noise-ratio improvement method, giving noise relative to system-noise temperature [17]. The noise temperature of the device is depicted in Fig. 7(b) on the bottom. As can be seen from the figure, the noise is close to the single-photon quantum limit over the 2-GHz bandwidth centered at 5 GHz, being 350 mK on average (1.45 photons). In the case of low pump power, the TWPA features broadband, flat gain profile, see Fig. 7(c). We operate the device in such a regime, because the entanglement is generated at low gain.

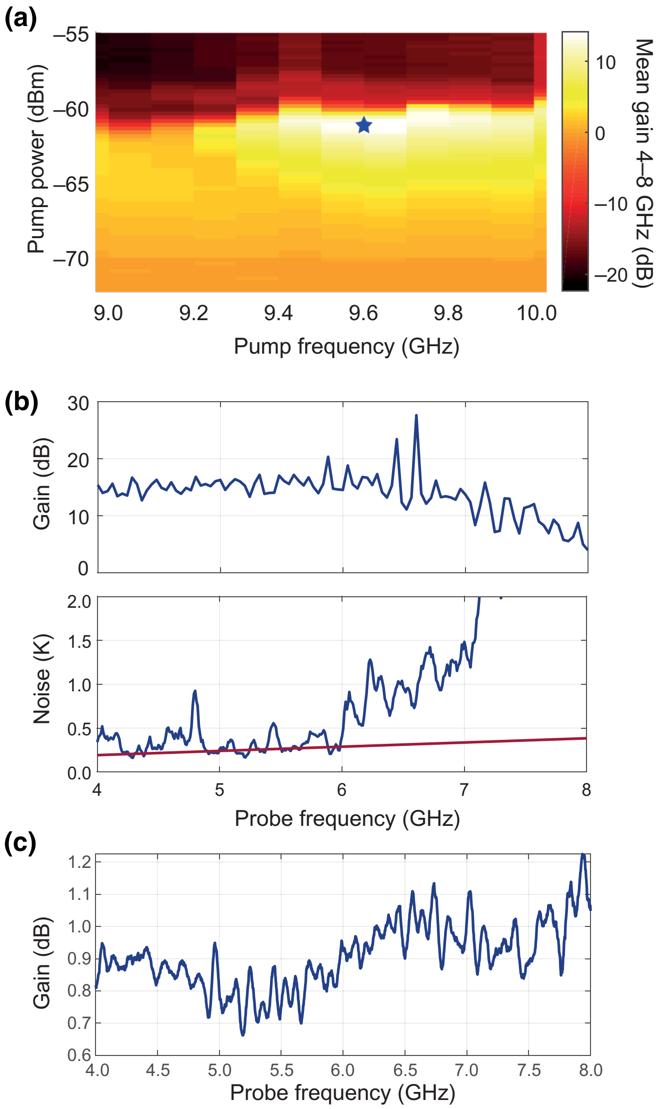

FIG. 7. (a) Mean gain for different pump powers and frequencies measured over 4–8-GHz range. dc-bias flux is $\Phi = 0.38\Phi_0$. The blue star marks the operation point where gain profile and noise temperature are measured. (b) Gain profile and noise temperature of TWPA over the 4–8-GHz range at the operating point marked in frame (a). While the TWPA provides 13 dB of gain on average, the noise temperature (blue line at the bottom) is close to the one-photon quantum limit (red line) $\hbar\omega/k_B$ over the 2-GHz bandwidth, with k_B as the Boltzmann constant. (c) Gain versus signal frequency at low pump power, which corresponds to the maximum entanglement generation.

The quantum efficiency [41] is then limited by the noise introduced by TWPA. Efficiency $\eta_e = 1/(1+N)$, where N is the number of added noise photons, is $\eta_e = 0.69$ in the case of high TWPA gain. It is impossible to characterize the added noise when the gain of TWPA is low in the exploited experimental setup.

APPENDIX E: NOISE CALIBRATION

The scheme for the system gain and noise calibration is presented on Fig. 3 in the main text. The calibration is done by measuring the power of the Johnson-Nyquist noise as a function of temperature. During the calibration we vary the noise power generated by components at 20-mK stage by changing the physical temperature of the whole stage. We assume that the output noise of the heated components is fully coupled to the impedance-matched measurement system. The Johnson-Nyquist noise power is given by $P(T) = \mathrm{BW} k_B G_{\mathrm{sys}}(T_N + T)$, where k_B is the Boltzmann constant, BW is the measurement bandwidth, which is 1 MHz in the experiment, and G_{sys} and T_{sys} are system gain and noise temperature that we aim to estimate. In order to determine the noise power, we measure the temperature-dependent variance of the output voltage, $\mathrm{Var}[V_{IQ}]$, which is captured at different temperatures using an Anritsu MS2830A Signal Analyzer. The same signal analyzer is used for the entanglement verification. The resulting noise power is given by $P(T) = \mathrm{Var}[V_{IQ}(T)]/Z_0$; here Z_0 is 50Ω.

We calculate the system-noise temperature by dividing the noise temperature in the case when TWPA is turned off $T_{N_{\mathrm{off}}}$ by the signal-to-noise-ratio improvement using the following formula [17]:

$$T_{\mathrm{sys}} = T_{N_{\mathrm{off}}} (\delta_{\mathrm{SNR}}^{-1} - G_T^{-1}), \tag{E1}$$

where δ_{SNR} is the signal-to-noise-ratio improvement and G_T is TWPA's gain.

In order to calibrate the I and Q variances for the entanglement verification, we measure the voltage variance when the TWPA is off and extract it from the variance measured in the case TWPA generates photons. Covariances are calculated by normalization per one photon. For the theoretical analysis, the measured voltage quadratures are calibrated and scaled according to the results of prior measurements of the system gain and noise temperature. Using a linear fit of the noise power as a function of temperature, we observe that in the case of unpumped TWPA $G_{\mathrm{off}} = 91.74 \pm 0.20$ dB (see pump-off case in Fig. 8) and $T_{\mathrm{sys}} = 4.75$ K. We observe that the gain varies with time and the variations are in the range of ±0.2 dB.

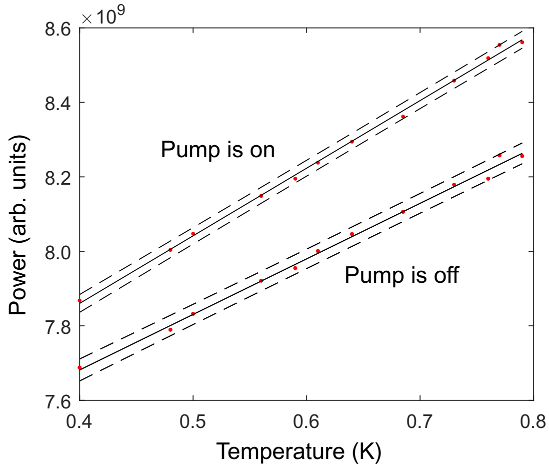

FIG. 8. Noise power at different temperatures: experiment (red dots), linear fit (solid black line), and variance (dashed black lines). The linear fit provides the system gain when TWPA is on G_{on} and gain when TWPA is off G_{off}, the difference of which gives the TWPA's gain of $G_T = 0.853$ dB.

APPENDIX F: LOSS MODEL: USING THE TWPA AS AN AMPLIFIER

To formulate a distributed model for a lossy waveguide with gain, a general mathematical description has been introduced in Ref. [72]. According to this model, each section of the waveguide contains loss per length $\mathcal{L}$ and gain per length $\mathcal{G}$. As the signal propagates along the device, noise will be added, it will get amplified, and will simultaneously decay into the loss channel (see Fig. 9). Considering the parametric dynamics of a general TWPA, this simple model is addressed further in Ref. [73], which is also employed in the following.

Consider perfect phase matching but include distributed loss with identical frequency independent coefficient κ along the TWPA. The Heisenberg-Langevin equation for the signal mode $\hat{a}_S$ and idler mode $\hat{a}_I$ inside the TWPA with the length L is then given by [73]

$$\begin{aligned}(\partial_t + v\partial_x)\hat{a}_S(x) &= \chi \hat{a}_I^\dagger(x) - \frac{\kappa}{2}\hat{a}_S(x) + \sqrt{\kappa}\hat{\xi}_S(x),\\ (\partial_t + v\partial_x)\hat{a}_I(x)^\dagger &= \chi \hat{a}_S(x) - \frac{\kappa}{2}\hat{a}_I^\dagger(x) + \sqrt{\kappa}\hat{\xi}_I^\dagger(x),\end{aligned} \tag{F1}$$

where v is the group velocity, χ is the parametric interaction strength, and $\hat{\xi}_i$ are noise mode sources. After moving to the frequency domain, one can find a scattering matrix $\mathbf{S}(x)$ linking the modes at the output of the TWPA, $x = L$, to those at $x = 0$ [73]:

$$\begin{aligned}(\hat{a}_s[L,\omega], \hat{a}_I^\dagger[L,\omega])^T &= \mathbf{S}(L)(\hat{a}_s[0,\omega], \hat{a}_I^\dagger[0,\omega])^T\\ &\quad + \frac{\sqrt{\kappa}}{v}\int_0^L dx'\, \mathbf{S}(L-x')(\hat{\xi}_s, \hat{\xi}_I^\dagger)^T,\end{aligned} \tag{F2}$$

where $(x,y)^T$ denotes a vertical vector with elements x and y. Here elements of the scattering matrix are given by

$$\begin{aligned}S_{11}(x) = S_{22}(x) &= e^{-\kappa\chi/2v + i\omega}\cosh\frac{\chi x}{v},\\ S_{12}(x) = S_{21}(x) &= e^{-\kappa\chi/2v + i\omega}\sinh\frac{\chi x}{v}.\end{aligned} \tag{F3}$$

This clearly represents simultaneous gain and loss along the TWPA. In the ideal case that the TPWA is lossless

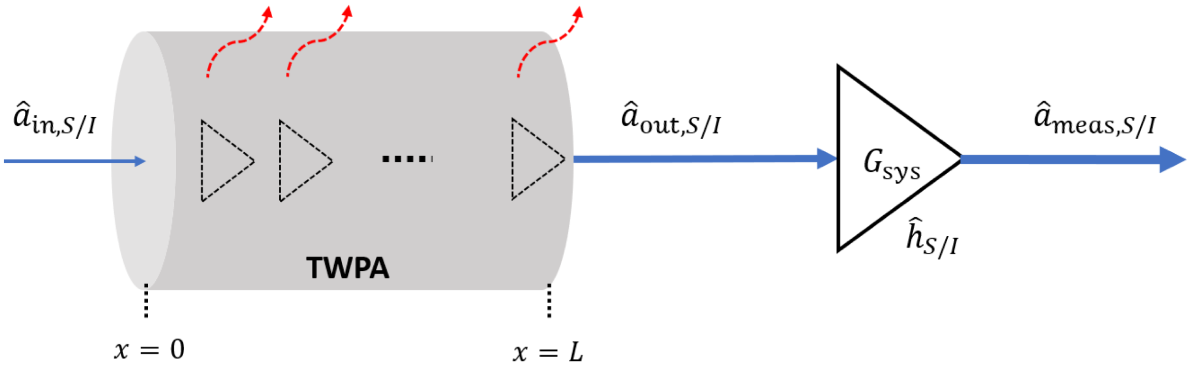
$\hat{a}_{\mathrm{in},S/I}$
TWPA
$x = 0$
$x = L$
$\hat{a}_{\mathrm{out},S/I}$
G_{sys}
$\hat{h}_{S/I}$
$\hat{a}_{\mathrm{meas},S/I}$

FIG. 9. Schematic description of the system chain. The TWPA is modeled by distributed gain and loss, which results in an effective power-dependent gain denoted by $G_T(P_p)$, with P_p denoting the power of the pump. The output modes of the TWPA include the two-mode squeezed vacuum plus added noise sources due to loss of the device. Before reaching the measurement stage, signals get amplified by the HEMT and room-temperature amplifiers (collectively described by the system gain G_{sys} and uncorrelated noise sources $\hat{h}_{S/I}$). Thus the combined gain of the system chain is described by $G_{\mathrm{on}}(P_p) = G_T(P_p)G_{\mathrm{sys}}$.

($\kappa = 0$), one recovers the well-known relation (excluding the global phase):

$$\hat{a}_S[L,\omega] = \cosh(r)\hat{a}_S[0,\omega] + \sinh(r)\hat{a}_I^\dagger[0,\omega], \qquad \text{(F4)}$$

with $r = \chi L/v$. However, when κ is nonzero the noise sources will be added to the propagating modes and couple due to the parametric interaction, i.e., noise added to the signal contributes to the idler mode and vice versa. For the sake of simplicity, one can adapt a lumped-element picture of Eq. (F2) to link the input and output signals of the TWPA. Assuming symmetric loss of signal and idler, one gets

$$\hat{a}_{\mathrm{out},S} = \sqrt{\eta G_S}\,\hat{a}_{\mathrm{in},S} + \sqrt{\eta G_I}\,\hat{a}_{\mathrm{in},I}^\dagger + \sqrt{G_S(1-\eta)}\,\hat{\xi}_S + \sqrt{G_I(1-\eta)}\,\hat{\xi}_I^\dagger, \qquad \text{(F5)}$$

where G_S and G_I describe the gain of the TWPA at signal and idler frequencies and η corresponds to its loss.

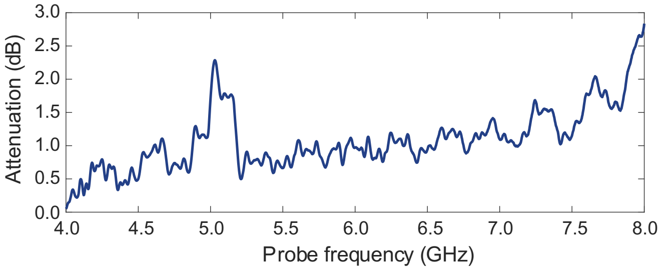

FIG. 10. Insertion losses of TWPA as a function of frequency of a probe signal obtained using a scheme with two microwave switches, which create one path through the TWPA and one through the superconducting coplanar line placed in the TWPA's sample holder. The coplanar line serves as a reference level that allows us to compare transmissions. The average insertion loss is −1.18 dB over the used bandwidth.

The internal losses of TWPA are modeled by the shunt capacitance loss tangent. From the process characterization of the atomic layer aluminum oxide deposition we estimate $\tan(\delta) = 0.0025$. The total loss in the waveguide is $e^{-\tan(\delta)\theta}$, where θ is electrical length of TWPA in radians. The estimated electrical length varies in range $\theta = 60 \pm 15$ rads at $\Phi_{\mathrm{dc}} = 0.38\Phi_0$ that gives $\eta = -0.65 \pm 0.20$ dB of internal losses that we use in the calibration.

Estimated loss value coincides with the one measured experimentally. In the device characterization experiment, two microwave switches are used in order to create two paths: one through the TWPA and one through the superconducting coplanar line placed in the same TWPA's sample holder. The coplanar line serves as a reference level for loss estimation. Over the whole 4–8-GHz bandwidth, the average internal loss $\eta \approx -1.18$ dB. During the broadband entanglement measurement, we normalize the covariance matrix using η, measured at each frequency (see Fig. 10).

APPENDIX G: ON-OFF CALIBRATION

In this section we discuss the on-off calibration technique for obtaining the covariance matrix of the output modes of the TWPA based on the covariance matrix of the measured signals at the end of the system [20,74]. We define $K = \{\hat{I}_S, \hat{Q}_S, \hat{I}_I, \hat{Q}_I\}$, where the quadratures are given by $\hat{I}_i = (\hat{a}_i + \hat{a}_i^\dagger)/2$ and $\hat{Q}_i = -i(\hat{a}_i - \hat{a}_i^\dagger)/2$, with the index $i = S, I$. We note that by considering these definitions of the quadratures we relate to the real and the imaginary parts of the field's amplitudes, which we actually measure in the experiment. Assuming zero-mean modes, our aim is to calibrate the covariance matrix with elements $V_{ij} = \langle \hat{K}_i\hat{K}_j + \hat{K}_j\hat{K}_i\rangle/2$ at the output of the TWPA since the covariance matrix fully characterizes the Gaussian states. We prove the Gaussian nature of the output signals by measuring the skewness $\langle \delta V_{IQ}^3\rangle/\sigma^3$ and kurtosis $\langle \delta V_{IQ}^4\rangle/\sigma^4$ of the signal V_{IQ}, where σ is the standard deviation and $\delta V_{IQ} = V_{IQ} - \langle V_{IQ}\rangle$. The observed skewness and kurtosis are 0.001 ± 0.005 and 2.998 ± 0.003, respectively, which proves the states are, indeed, Gaussian states.

Suppose that the competition between distributed loss and gain along the TWPA results in an effective power-dependent gain $G_T(P_p)$, such that by referring to Eq. (F5) one finds $G_T(P_p) := \eta G_S$. Thus, when the TWPA is pumped the gain can compensate the loss and one has $G_T(P_p) > 1$. However, when the pump is off the loss can not be compensated and we get the attenuation $G_T(P_p = 0) < 1$. Assuming that the input of the TWPA are vacuum fields $\hat v_{S/I}$, the measured fields in presence of pump ($P_p \neq 0$) read

$$\hat a^{(\text{on})}_{\text{meas},S} = \sqrt{G_{\text{sys}}}\left(\sqrt{\eta G_S}\;\hat v_S + \sqrt{\eta G_I}\;\hat v_I^\dagger + \sqrt{G_S(1-\eta)}\;\hat\xi_S + \sqrt{G_I(1-\eta)}\;\hat\xi_I^\dagger\right) + \sqrt{G_{\text{sys}}-1}\hat h_S^\dagger, \tag{G1}$$

$$\hat a^{(\text{on})}_{\text{meas},I} = \sqrt{G_{\text{sys}}}\left(\sqrt{\eta G_I}\;\hat v_I + \sqrt{\eta G_S}\;\hat v_S^\dagger + \sqrt{G_I(1-\eta)}\;\hat\xi_I + \sqrt{G_S(1-\eta)}\;\hat\xi_S^\dagger\right) + \sqrt{G_{\text{sys}}-1}\hat h_I^\dagger. \tag{G2}$$

If the TWPA is not pumped, then the overall gain of the TWPA is described by the attenuation $G_T(P_p = 0) = \eta$. Considering the noise sources $\hat\zeta_{S/I}$ added due to this attenuation, one obtains

$$\hat a^{(\text{off})}_{\text{meas},S} = \sqrt{G_{\text{sys}}\eta}\;\hat v_S + \sqrt{G_{\text{sys}}\,(1-\eta)}\;\hat\zeta_S + \sqrt{G_{\text{sys}}-1}\hat h_S^\dagger, \tag{G3}$$

$$\hat a^{(\text{off})}_{\text{meas},I} = \sqrt{G_{\text{sys}}\eta}\;\hat v_I + \sqrt{G_{\text{sys}}\,(1-\eta)}\;\hat\zeta_I + \sqrt{G_{\text{sys}}-1}\hat h_I^\dagger. \tag{G4}$$

In further analysis of variances and covariances, we omit all coefficients in normalization $\mathcal{N}$ except for the gain. Thus, subtracting the covariance matrix of the measured quadratures when the pump is on from the covariance matrix of the measured quadratures when the pump is off yields

$$\mathbf{V}^{(\text{on})}_{\text{meas}} - \mathbf{V}^{(\text{off})}_{\text{meas}} = G_{\text{sys}}\mathbf{V}_{\text{out}} - \frac{G_{\text{sys}}\eta}{4}\mathcal{I}_4 - G_{\text{sys}}(1-\eta)\mathbf{V}_{\text{noise}}, \tag{G5}$$

where $\mathbf{V}_{\text{out}}$ denotes the covariance matrix of the output modes of TWPA, the identity matrix is related to the covariance matrix of the vacuum inputs, and $\mathbf{V}_{\text{noise}}$ denotes the added noise of the unpumped TWPA due to its loss. Accordingly, one finds

$$\mathbf{V}_{\text{out}} = \frac{\mathbf{V}^{(\text{on})}_{\text{meas}} - \mathbf{V}^{(\text{off})}_{\text{meas}}}{G_{\text{sys}}} + \frac{\eta}{4}\mathcal{I}_4 + (1-\eta)\mathbf{V}_{\text{noise}}. \tag{G6}$$

Recalling that $\eta = G_T(P_p = 0)$, $G_{\text{off}} = \eta G_{\text{sys}}$ and assuming perfect thermalization for the TWPA's noise sources in Eqs. (G3) and (G4), we obtain

$$\mathbf{V}_{\text{out}} = \frac{\eta\left(\mathbf{V}^{(\text{on})}_{\text{meas}} - \mathbf{V}^{(\text{off})}_{\text{meas}}\right)}{G_{\text{off}}} + \frac{1}{4}\mathcal{I}_4. \tag{G7}$$

By returning back all normalization coefficients, in addition to multiplying $\mathbf{V}_{\text{out}}$ by a factor 4—to rescale the vacuum fluctuations to 1 (instead of 1/4)—we get the expressions given in Eq. (3) of the main text.

APPENDIX H: ERROR ANALYSIS

The two main sources of error in the estimation of entanglement strength and squeezing are inaccuracies in the gain of the system and in the internal losses of the TWPA. The system gain is $G_{\text{off}} = 91.74 \pm 0.20$ dB and the loss coefficient is $\eta = -0.65 \pm 0.20$ dB. This gives an uncertainty of ± 0.4 dB for the normalization coefficient $\mathcal{N}$. Taking the highest squeezing point we obtain $\nu = 0.55 \pm 0.10$, which is given by the error in normalization coefficients.

APPENDIX I: RATE OF ENTANGLEMENT GENERATION AND PURITY

To quantify the entanglement generation rate of TWPA we introduce $R_E = 2\langle \mathcal{I}_1^2\rangle E_F(\Delta\omega + \delta\omega)$. The photon flux intensity $\langle \mathcal{I}_1^2\rangle$ is extracted directly from the experiment and $(\Delta\omega + \delta\omega)$ is set manually. The entropy of formation E_F according to Refs. [75,76] can be calculated from the symplectic eigenvalue using the following relation:

$$E_F = c_+ \log c_+ - c_- \log c_-, \tag{I1}$$

where $c_\pm = (\nu_{\text{min}}^{-1/2} \pm \nu_{\text{min}}^{1/2})/4$.

The purity of the quantum state is calculated from the covariance matrix $\mathbf{V}_{\text{out}}$: $\mu = 1/\sqrt{|\det(\mathbf{V}_{\text{out}})|}$, where det is the matrix determinant.

APPENDIX J: SINGLE-MODE SQUEEZING

Besides two-mode entanglement that we characterize with the covariance matrix depicted in Fig. 11(a), we demonstrate the generation of single-mode squeezed states. For this experiment, we consider a spanned single mode with the 0.5-MHz bandwidth centered at $\omega_p/2$. The parametric amplifier operates in the degenerate mode at this point. These amplitudes are shown in Fig. 11(b) as a

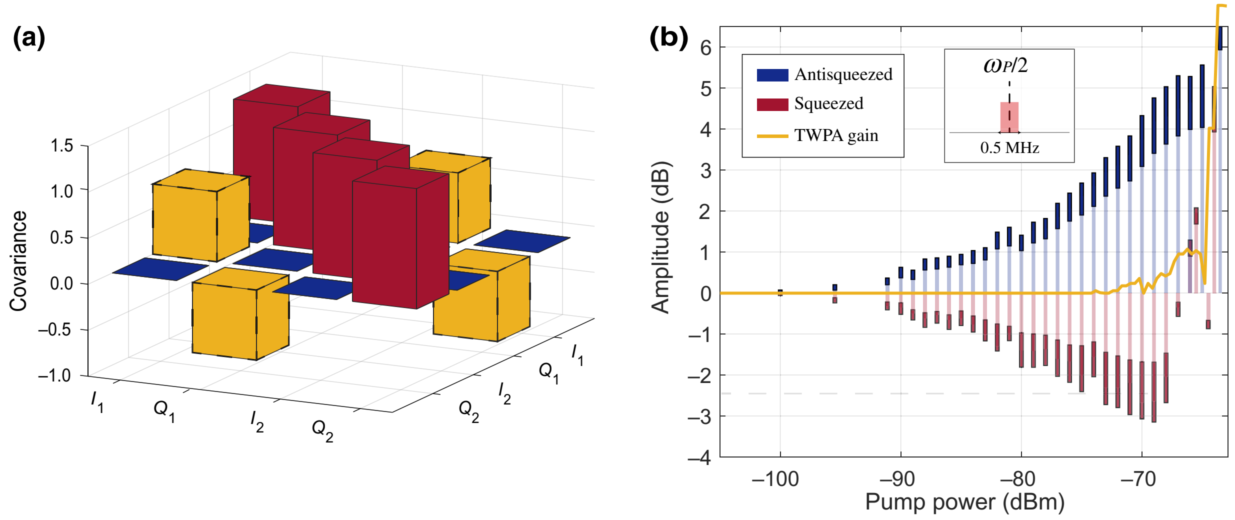

FIG. 11. (a) The covariance matrix for the two-mode entangled state. (b) The single-mode squeezing for different pump powers. Transparent blue bars corresponds to the measured amplified quadrature, while transparent red bars corresponds to the measured squeezed quadrature. The solid red and blue bars correspond to the errors in the amplitude estimation. The yellow curve shows the gain of the TWPA.

function of the pump power. The maximum squeezing of 2.4 ± 0.7 dB is achieved at −68-dBm pump power.

[1] T. Brecht, W. Pfaff, C. Wang, Y. Chu, L. Frunzio, M. H. Devoret, and R. J. Schoelkopf, Multilayer microwave integrated quantum circuits for scalable quantum computing, npj Quantum Inf. **2**, 16002 (2016).

[2] P. Magnard, S. Storz, P. Kurpiers, J. Schär, F. Marxer, J. Lütolf, T. Walter, J.-C. Besse, M. Gabureac, K. Reuer, A. Akin, B. Royer, A. Blais, and A. Wallraff, Microwave Quantum Link Between Superconducting Circuits Housed in Spatially Separated Cryogenic Systems, Phys. Rev. Lett. **125**, 260502 (2020).

[3] L. D. Burkhart, J. D. Teoh, Y. Zhang, C. J. Axline, L. Frunzio, M. Devoret, L. Jiang, S. Girvin, and R. Schoelkopf, Error-Detected State Transfer and Entanglement in a Superconducting Quantum Network, PRX Quantum **2**, 030321 (2021).

[4] S. Lloyd, Enhanced sensitivity of photodetection via quantum illumination, Science **321**, 1463 (2008).

[5] S. Barzanjeh, S. Guha, C. Weedbrook, D. Vitali, J. H. Shapiro, and S. Pirandola, Microwave Quantum Illumination, Phys. Rev. Lett. **114**, 080503 (2015).

[6] S. Pogorzalek, K. G. Fedorov, M. Xu, A. Parra-Rodriguez, M. Sanz, M. Fischer, E. Xie, K. Inomata, Y. Nakamura, E. Solano, A. Marx, F. Deppe, and R. Gross, Secure quantum remote state preparation of squeezed microwave states, Nat. Commun. **10**, 2604 (2019).

[7] R. Di Candia, H. Yiğitler, G. Paraoanu, and R. Jäntti, Two-Way Covert Quantum Communication in the Microwave Regime, PRX Quantum **2**, 020316 (2021).

[8] K. G. Fedorov, M. Renger, S. Pogorzalek, R. Di Candia, Q. Chen, Y. Nojiri, K. Inomata, Y. Nakamura, M. Partanen, and A. Marx, *et al.*, Experimental quantum teleportation of propagating microwaves, Sci. Adv. **7**, eabk0891 (2021).

[9] B. Yurke, P. G. Kaminsky, R. E. Miller, E. A. Whittaker, A. D. Smith, A. H. Silver, and R. W. Simon, Observation of 4.2-K Equilibrium-Noise Squeezing via a Josephson-Parametric Amplifier, Phys. Rev. Lett. **60**, 764 (1988).

[10] T. Yamamoto, K. Inomata, M. Watanabe, K. Matsuba, T. Miyazaki, W. D. Oliver, Y. Nakamura, and J. S. Tsai, Flux-driven Josephson parametric amplifier, Appl. Phys. Lett. **93**, 042510 (2008).

[11] M. Hatridge, R. Vijay, D. H. Slichter, J. Clarke, and I. Siddiqi, Dispersive magnetometry with a quantum limited SQUID parametric amplifier, Phys. Rev. B **83**, 134501 (2011).

[12] P. Lähteenmäki, V. Vesterinen, J. Hassel, H. Seppä, and P. Hakonen, Josephson junction microwave amplifier in self-organized noise compression mode, Sci. Rep. **2**, 276 (2012).

[13] J. Y. Mutus, *et al.*, Design and characterization of a lumped element single-ended superconducting microwave parametric amplifier with on-chip flux bias line, Appl. Phys. Lett. **103**, 122602 (2013).

[14] P. Lähteenmäki, V. Vesterinen, J. Hassel, G. S. Paraoanu, H. Seppä, and P. Hakonen, Advanced concepts in Josephson junction reflection amplifiers, J. Low Temp. Phys. **175**, 868 (2014).

[15] J. Y. Mutus, T. C. White, R. Barends, Y. Chen, Z. Chen, B. Chiaro, A. Dunsworth, E. Jeffrey, J. Kelly, A. Megrant, C. Neill, P. J. J. O'Malley, P. Roushan, D. Sank, A. Vainsencher, J. Wenner, K. M. Sundqvist, A. N. Cleland, and J. M. Martinis, Strong environmental coupling in a Josephson parametric amplifier, Appl. Phys. Lett. **104**, 263513 (2014).

[16] X. Zhou, V. Schmitt, P. Bertet, D. Vion, W. Wustmann, V. Shumeiko, and D. Esteve, High-gain weakly nonlinear

flux-modulated Josephson parametric amplifier using a squid array, Phys. Rev. B **89**, 214517 (2014).

[17] T. Roy, S. Kundu, M. Chand, A. M. Vadiraj, A. Ranadive, N. Nehra, M. P. Patankar, J. Aumentado, A. A. Clerk, and R. Vijay, Broadband parametric amplification with impedance engineering: Beyond the gain-bandwidth product, Appl. Phys. Lett. **107**, 262601 (2015).

[18] S. Jebari, F. Blanchet, A. Grimm, D. Hazra, R. Albert, P. Joyez, D. Vion, D. Estève, F. Portier, and M. Hofheinz, Near-quantum-limited amplification from inelastic Cooper-pair tunnelling, Nat. Electron. **1**, 223 (2018).

[19] T. Elo, T. S. Abhilash, M. R. Perelshtein, I. Lilja, E. V. Korostylev, and P. J. Hakonen, Broadband lumped-element Josephson parametric amplifier with single-step lithography, Appl. Phys. Lett. **114**, 152601 (2019).

[20] C. Eichler, D. Bozyigit, C. Lang, M. Baur, L. Steffen, J. M. Fink, S. Filipp, and A. Wallraff, Observation of Two-Mode Squeezing in the Microwave Frequency Domain, Phys. Rev. Lett. **107**, 113601 (2011).

[21] C. M. Wilson, G. Johansson, A. Pourkabirian, M. Simoen, J. R. Johansson, T. Duty, F. Nori, and P. Delsing, Observation of the dynamical Casimir effect in a superconducting circuit, Nature **479**, 376 (2011).

[22] L. Zhong, E. P. Menzel, R. D. Candia, P. Eder, M. Ihmig, A. Baust, M. Haeberlein, E. Hoffmann, K. Inomata, T. Yamamoto, Y. Nakamura, E. Solano, F. Deppe, A. Marx, and R. Gross, Squeezing with a flux-driven Josephson parametric amplifier, New J. Phys. **15**, 125013 (2013).

[23] P. Lähteenmäki, G. S. Paraoanu, J. Hassel, and P. J. Hakonen, Coherence and multimode correlations from vacuum fluctuations in a microwave superconducting cavity, Nat. Commun. **7**, 12548 (2016).

[24] A. L. Grimsmo and A. Blais, Squeezing and quantum state engineering with Josephson travelling wave amplifiers, npj Quantum Inf. **3**, 1 (2017).

[25] B. H. Schneider, A. Bengtsson, I. M. Svensson, T. Aref, G. Johansson, J. Bylander, and P. Delsing, Observation of Broadband Entanglement in Microwave Radiation from a Single Time-Varying Boundary Condition, Phys. Rev. Lett. **124**, 140503 (2020).

[26] C. Macklin, K. O'Brien, D. Hover, M. E. Schwartz, V. Bolkhovsky, X. Zhang, W. D. Oliver, and I. Siddiqi, A near-quantum-limited Josephson traveling-wave parametric amplifier, Science **350**, 307 (2015).

[27] T. C. White, *et al.*, Traveling wave parametric amplifier with Josephson junctions using minimal resonator phase matching, Appl. Phys. Lett. **106**, 242601 (2015).

[28] A. B. Zorin, Josephson Traveling-Wave Parametric Amplifier with Three-Wave Mixing, Phys. Rev. Appl. **6**, 034006 (2016).

[29] S. Krinner, S. Storz, P. Kurpiers, P. Magnard, J. Heinsoo, R. Keller, J. Lütolf, C. Eichler, and A. Wallraff, Engineering cryogenic setups for 100-qubit scale superconducting circuit systems, EPJ Quantum Technol. **6**, 2 (2019).

[30] Y. Cai, J. Roslund, G. Ferrini, F. Arzani, X. Xu, C. Fabre, and N. Treps, Multimode entanglement in reconfigurable graph states using optical frequency combs, Nat. Commun. **8**, 1 (2017).

[31] M. Esposito, A. Ranadive, L. Planat, and N. Roch, Perspective on traveling wave microwave parametric amplifiers, Appl. Phys. Lett. **119**, 120501 (2021).

[32] V. Vesterinen and J. Hassel, Josephson traveling wave parametric amplifier, WO 2020/152393 A1 (2020).

[33] N. E. Frattini, U. Vool, S. Shankar, A. Narla, K. M. Sliwa, and M. H. Devoret, 3-wave mixing Josephson dipole element, Appl. Phys. Lett. **110**, 222603 (2017).

[34] B. Yurke and E. Buks, Performance of cavity-parametric amplifiers, employing Kerr nonlinearites, in the presence of two-photon loss, J. Lightwave Technol. **24**, 5054 (2006).

[35] Y. Krupko, V. D. Nguyen, T. Weißl, É. Dumur, J. Puertas, R. Dassonneville, C. Naud, F. W. J. Hekking, D. M. Basko, O. Buisson, N. Roch, and W. Hasch-Guichard, Kerr nonlinearity in a superconducting Josephson metamaterial, Phys. Rev. B **98**, 094516 (2018).

[36] L. Planat, A. Ranadive, R. Dassonneville, J. Puertas Martínez, S. Léger, C. Naud, O. Buisson, W. Hasch-Guichard, D. M. Basko, and N. Roch, Photonic-Crystal Josephson Traveling-Wave Parametric Amplifier, Phys. Rev. X **10**, 021021 (2020).

[37] G. Agrawal, *Nonlinear Fiber Optics* (Elsevier, Berlin, 2013).

[38] M. Malnou, M. Vissers, J. Wheeler, J. Aumentado, J. Hubmayr, J. Ullom, and J. Gao, Three-Wave Mixing Kinetic Inductance Traveling-Wave Amplifier with Near-Quantum-Limited Noise Performance, PRX Quantum **2**, 010302 (2021).

[39] A. Ranadive, M. Esposito, L. Planat, E. Bonet, C. Naud, O. Buisson, W. Guichard, and N. Roch, Kerr reversal in Josephson meta-material and traveling wave parametric amplification, Nat. Commun. **13**, 1 (2022).

[40] M. T. Bell and A. Samolov, Traveling-Wave Parametric Amplifier Based on a Chain of Coupled Asymmetric SQUIDs, Phys. Rev. Appl. **4**, 024014 (2015).

[41] S. Boutin, D. M. Toyli, A. V. Venkatramani, A. W. Eddins, I. Siddiqi, and A. Blais, Effect of Higher-Order Nonlinearities on Amplification and Squeezing in Josephson Parametric Amplifiers, Phys. Rev. Appl. **8**, 054030 (2017).

[42] K. Peng, M. Naghiloo, J. Wang, G. D. Cunningham, Y. Ye, and K. P. O'Brien, Floquet-Mode Traveling-Wave Parametric Amplifiers, PRX Quantum **3**, 020306 (2022).

[43] L. Grönberg, M. Kiviranta, V. Vesterinen, J. Lehtinen, S. Simbierowicz, J. Luomahaara, M. Prunnila, and J. Hassel, Side-wall spacer passivated sub-μm Josephson junction fabrication process, Supercond. Sci. Technol. **30**, 125016 (2017).

[44] S. Simbierowicz, V. Vesterinen, J. Milem, A. Lintunen, M. Oksanen, L. Roschier, L. Grönberg, J. Hassel, D. Gunnarsson, and R. E. Lake, Characterizing cryogenic amplifiers with a matched temperature-variable noise source, Rev. Sci. Instrum. **92**, 034708 (2021).

[45] K. R. Parameswaran, J. R. Kurz, R. V. Roussev, and M. M. Fejer, Observation of 99% pump depletion in single-pass second-harmonic generation in a periodically poled lithium niobate waveguide, Opt. Lett. **27**, 43 (2002).

[46] V. Vesterinen and S. Simbierowicz, Traveling wave parametric amplifier PCT/FI2021/050283 (2021).

[47] T. Dixon, J. Dunstan, G. Long, J. Williams, P. Meeson, and C. Shelly, Capturing Complex Behavior in Josephson Traveling-Wave Parametric Amplifiers, Phys. Rev. Appl. **14**, 034058 (2020).

[48] R. DeSalvo, H. Vanherzeele, D. J. Hagan, M. Sheik-Bahae, G. Stegeman, and E. W. V. Stryland, Self-focusing and self-defocusing by cascaded second-order effects in KTP, Opt. Lett. **17**, 28 (1992).

[49] C. C. Bultink, B. Tarasinski, N. Haandbæk, S. Poletto, N. Haider, D. J. Michalak, A. Bruno, and L. DiCarlo, General method for extracting the quantum efficiency of dispersive qubit readout in circuit QED, Appl. Phys. Lett. **112**, 092601 (2018).

[50] S. L. Braunstein and P. van Loock, Quantum information with continuous variables, Rev. Mod. Phys. **77**, 513 (2005).

[51] G. Adesso, S. Ragy, and A. R. Lee, Continuous variable quantum information: Gaussian states and beyond, Open Syst. Inf. Dyn. **21**, 1440001 (2014).

[52] A. Peres, Separability Criterion for Density Matrices, Phys. Rev. Lett. **77**, 1413 (1996).

[53] P. Horodecki, Separability criterion and inseparable mixed states with positive partial transposition, Phys. Lett. A **232**, 333 (1997).

[54] R. Simon, Peres-Horodecki Separability Criterion for Continuous Variable Systems, Phys. Rev. Lett. **84**, 2726 (2000).

[55] G. Vidal and R. F. Werner, Computable measure of entanglement, Phys. Rev. A **65**, 032314 (2002).

[56] K. Audenaert, M. B. Plenio, and J. Eisert, Entanglement Cost under Positive-Partial-Transpose-Preserving Operations, Phys. Rev. Lett. **90**, 027901 (2003).

[57] C. W. Sandbo Chang, M. Simoen, J. Aumentado, C. Sabín, P. Forn-Díaz, A. M. Vadiraj, F. Quijandría, G. Johansson, I. Fuentes, and C. M. Wilson, Generating Multimode Entangled Microwaves with a Superconducting Parametric Cavity, Phys. Rev. Appl. **10**, 044019 (2018).

[58] M. G. A. Paris, F. Illuminati, A. Serafini, and S. De Siena, Purity of Gaussian states: Measurement schemes and time evolution in noisy channels, Phys. Rev. A **68**, 012314 (2003).

[59] C. H. Bennett, D. P. DiVincenzo, J. A. Smolin, and W. K. Wootters, Mixed-state entanglement and quantum error correction, Phys. Rev. A **54**, 3824 (1996).

[60] S. Lloyd and S. L. Braunstein, Quantum Computation over Continuous Variables, Phys. Rev. Lett. **82**, 1784 (1999).

[61] S. D. Bartlett and B. C. Sanders, Universal continuous-variable quantum computation: Requirement of optical nonlinearity for photon counting, Phys. Rev. A **65**, 042304 (2002).

[62] R. Yanagimoto, T. Onodera, E. Ng, L. G. Wright, P. L. McMahon, and H. Mabuchi, Engineering a Kerr-Based Deterministic Cubic Phase Gate via Gaussian Operations, Phys. Rev. Lett. **124**, 240503 (2020).

[63] K. V. Petrovnin, M. R. Perelshtein, I. Lilja, T. Korkalainen, V. Vesterinen, G. S. Paraoanu, and P. J. Hakonen, Generation and structuring of multipartite entanglement in Josephson parametric system, (to be published) (2021).

[64] T. Hillmann, F. Quijandría, G. Johansson, A. Ferraro, S. Gasparinetti, and G. Ferrini, Universal Gate Set for Continuous-Variable Quantum Computation with Microwave Circuits, Phys. Rev. Lett. **125**, 160501 (2020).

[65] E. Samsonov, R. Goncharov, A. Gaidash, A. Kozubov, V. Egorov, and A. Gleim, Subcarrier wave continuous variable quantum key distribution with discrete modulation: Mathematical model and finite-key analysis, Sci. Rep. **10**, 10034 (2020).

[66] X. Guo, C. R. Breum, J. Borregaard, S. Izumi, M. V. Larsen, T. Gehring, M. Christandl, J. S. Neergaard-Nielsen, and U. L. Andersen, Distributed quantum sensing in a continuous-variable entangled network, Nat. Phys. **16**, 281 (2019).

[67] K. M. Backes, *et al.*, A quantum enhanced search for dark matter axions, Nature **590**, 238 (2021).

[68] M. Esposito, A. Ranadive, L. Planat, S. Leger, D. Fraudet, V. Jouanny, O. Buisson, W. Guichard, C. Naud, J. Aumentado, F. Lecocq, and N. Roch, Observation of Two-Mode Squeezing in a Traveling Wave Parametric Amplifier, Phys. Rev. Lett. **128**, 153603 (2022).

[69] J. Y. Qiu, A. Grimsmo, K. Peng, B. Kannan, B. Lienhard, Y. Sung, P. Krantz, V. Bolkhovsky, G. Calusine, D. Kim, A. Melville, B. M. Niedzielski, J. Yoder, M. E. Schwartz, T. P. Orlando, I. Siddiqi, S. Gustavsson, K. P. O'Brien, and W. D. Oliver, Broadband squeezed microwaves and amplification with a Josephson traveling-wave parametric amplifier (2022), ArXiv:2201.11261.

[70] C. Yan, J. Hassel, V. Vesterinen, J. Zhang, J. Ikonen, L. Grönberg, J. Goetz, and M. Möttönen, A low-noise on-chip coherent microwave source, Nat. Electron. **4**, 885 (2021).

[71] N. E. Frattini, V. V. Sivak, A. Lingenfelter, S. Shankar, and M. H. Devoret, Optimizing the Nonlinearity and Dissipation of a SNAIL Parametric Amplifier for Dynamic Range, Phys. Rev. Appl. **10**, 054020 (2018).

[72] H. A. Haus, *Electromagnetic Noise and Quantum Optical Measurements* (Springer Berlin Heidelberg, New York, 2000).

[73] M. Houde, L. Govia, and A. Clerk, Loss Asymmetries in Quantum Traveling-Wave Parametric Amplifiers, Phys. Rev. Appl. **12**, 034054 (2019).

[74] E. Flurin, N. Roch, J. D. Pillet, F. Mallet, and B. Huard, Superconducting Quantum Node for Entanglement and Storage of Microwave Radiation, Phys. Rev. Lett. **114**, 090503 (2015).

[75] J. Laurat, T. Coudreau, G. Keller, N. Treps, and C. Fabre, Effects of mode coupling on the generation of quadrature Einstein-Podolsky-Rosen entanglement in a type-II optical parametric oscillator below threshold, Phys. Rev. A **71**, 022313 (2005).

[76] E. Flurin, N. Roch, F. Mallet, M. H. Devoret, and B. Huard, Generating Entangled Microwave Radiation over Two Transmission Lines, Phys. Rev. Lett. **109**, 183901 (2012).